RSC Advances

ARTICLE TYPE

Facile Preparation of CuO@SnO₂ Nanobelts as a High-Capacity and Long-Life Anode for Lithium-Ion Batteries

Xiaoshu Zhu, Huimin Shi, Jinwei Yin, Huimin Zhu, Yiming Zhou, Yawen Tang, Ping Wu* and Tianhong Lu

A novel type of one-dimensional (1D) nanohybrid of SnO₂ and transition-metal oxides, i.e. CuO nanobelts decorated with SnO₂ nanocrystals (CuO@SnO₂ nanobelts), has been ₁₀ constructed *via* a facile hydrothermal approach by using CuO nanobelts as templates. The as-prepared CuO@SnO₂ nanobelts has been applied as a potential anode material for lithium-ion batteries (LIBs), and exhibits markedly enhanced lithium-storage capabilities in terms of specific capacity and ₁₅ cycling stability compared with single CuO and SnO₂ counterparts. The synergistic effects between CuO and SnO₂ together with the unique 1D belt-like nanostructure could be responsible for its high capacity and remarkable capacity retention. The facile synthetic approach and superior lithium-₂₀ storage capabilities of CuO@SnO₂ nanobelts make it an ideal anodic candidate for advanced LIBs with high energy density and long cycle life.

Since the pioneering work reported in 1997 by Miyasaka et al.,[1] tin-based materials including tin alloys, tin oxides, tin sulfides, ₂₅ and so forth have emerged as an important anodic category for lithium-ion batteries (LIBs).[2-9] Among them, tin dioxide (SnO₂) has been considered to be ideal anodic candidate to replace commercial graphite-based materials owing to its high safety, specific capacity, and ease of preparation.[10-29] However, the ₃₀ practical application of SnO₂ has been greatly hampered by the poor anodic performances in terms of cycling stability and so forth, which intrinsically originate from its Li-storage mechanism. Generally, the lithium storage behavior of SnO₂ can be described as follows: $SnO_2 + 4Li^+ + 4e^- \rightarrow Sn + 2Li_2O$ (eq 1); $Sn + 4.4Li^+ +$ ₃₅ $4.4e^- \leftrightarrow Li_{4.4}Sn$ (eq 2).[10] The alloying and de-alloying processes described by eq 2 give rise to huge volume changes (~300%), progressive pulverization, and fast capacity fading, whereas the formation of inactive Li_2O described by eq 1 leads to the large lithium consumption and irreversible capacity.

₄₀ Up to now, substantial research efforts have been devoted to address the aforementioned issues starting from the structural and compositional design of the anodic systems, and nanostructuring and hybridizing SnO₂ materials with various matrixes have proved to be effective design strategies for improved Li-storage ₄₅ performances.[11-29] On one hand, various nanostructures especially one-dimensional (1D) nanostructures have demonstrated improved anodic performances owing to their large surface area and fast charge transport pathways.[11-14] On the other hand, the hybrids of SnO₂ and transition-metal oxides (M$_x$O$_y$, M = Fe, Co, ₅₀ Ni, Cu, Mo, W, etc) have proven their superiorities compared with single-component oxides due to their synergistic effects on lithium storage, which can be specified as follows.[20-29] The stepwise Li-storage processes at different potentials of SnO₂ and M$_x$O$_y$ can accommodate the volume variations and thus improve ₅₅ the cycling performance of the hybrids, whereas the *in situ* generated transition-metal nanoparticles from M$_x$O$_y$ component can activate/promote the oxidation of metallic tin, reversible formation/decomposition of polymeric gel-like film, and increase the overall capacity of the hybrids.[20-31] Therefore, the 1D ₆₀ nanohybrids of SnO₂ and M$_x$O$_y$ are expected to display prominent Li-storage performances and serve as advanced anodes for LIBs in electric vehicles and smart grids by virtue of their unique structural and compositional features.

Herein, a novel type of 1D nanohybrid of SnO₂ and M$_x$O$_y$, i.e. ₆₅ CuO nanobelts decorated with SnO₂ nanocrystals (CuO@SnO₂ nanobelts), has been designed and synthesized *via* a facile hydrothermal method by using CuO nanobelts as templates. The as-prepared CuO@SnO₂ nanobelts has been applied as a potential anode material for LIBs, and exhibits much higher capacities and ₇₀ markedly improved cycling stability compared with bare CuO nanobelts and SnO₂ nanocrystals.
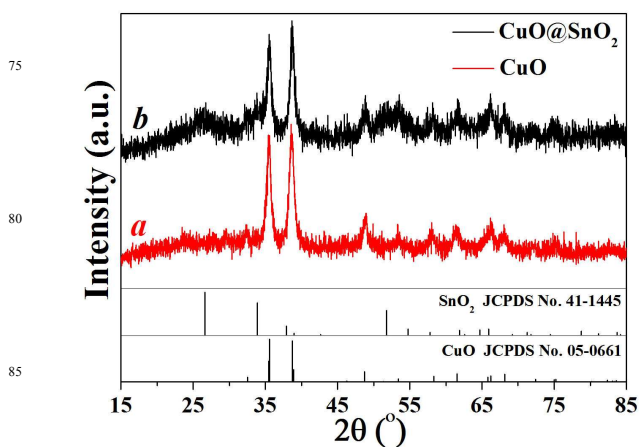
Fig. 1 XRD patterns of CuO nanobelts (curve *a*) and CuO@SnO₂ ₉₀ nanobelts (curve *b*).

The crystalline state of the samples was examined by X-ray powder diffraction (XRD) (Fig. 1). As can be seen, the diffraction peaks from curves *a* and *b* could be indexed to monoclinic CuO (JCPDS No. 05-0661) and tetragonal SnO_2 (JCPDS No. 41-1445), respectively. The crystalline phases change from CuO in the template and mixed phases of CuO and SnO_2 in the final products, confirming the formation of CuO and $CuO@SnO_2$ nanobelts. Additionally, the differences in sharpness of these two sets of diffraction peaks originate from the different crystalline sizes of CuO and SnO_2.
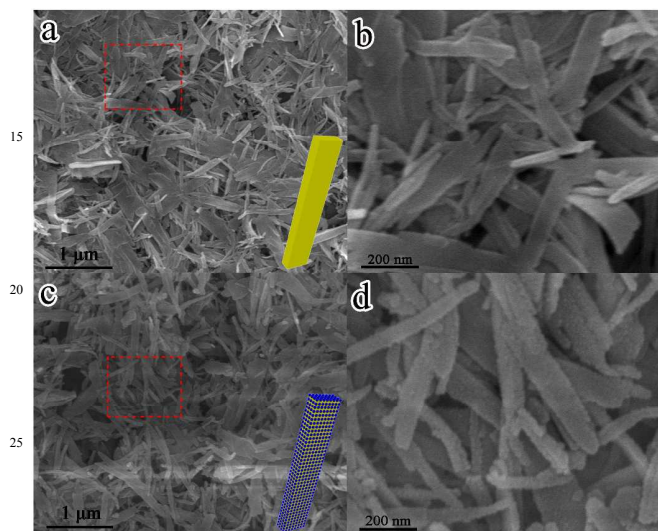
Fig. 2 SEM images of CuO nanobelts (a,b) and $CuO@SnO_2$ nanobelts (c,d). Insets in (a) and (c) are their corresponding models.

Fig. 2 displays the scanning electron microscopy (SEM) images of CuO and $CuO@SnO_2$ nanobelts with their corresponding models. As observed, the CuO template displays a typical belt-like morphology with a smooth surface (Fig. 2a and b), and the nanobelt is single-crystalline in nature (Fig. S1, ESI†). After the coating of SnO_2 layer, the belt-like morphology is well preserved, and the surface of the nanobelts become much rougher due to the decoration of uniform SnO_2 nanocrystals (Fig. 2c and d). For comparison, bare SnO_2 sample has been prepared through the same approach but without CuO templates, and exists in the form of porous nanospheres (Fig. S2, ESI†).

The morphological, structural and compositional features of $CuO@SnO_2$ nanobelts were further characterized by transmission electron microscopy (TEM) and high-resolution TEM (HRTEM) (Fig. 3). As can be seen from the TEM image (Fig. 3a), the $CuO@SnO_2$ product exists in the form of core–shelled nanobelts, and no isolated SnO_2 nanocrystals can be observed in the sample except for the surface of the nanobelts. The magnified TEM image of a single nanobelt clearly demonstrate that the SnO_2 layer consisting of numerous nanocrystals is uniformly and densely coated on the surface of CuO nanobelt (Fig. 3b). Additionally, the selected-area electron diffraction (SAED) pattern shows typical diffraction spots characteristic of (110), (-110), and (020) planes of CuO and diffraction rings related to (110), (101), and (211) planes SnO_2, further suggesting the formation of single-crystalline CuO nanobelt decorated with

numerous SnO_2 nanocrystals. Fig. 3c displays the energy-dispersive X-ray spectrometer (EDS) spectrum of the product. The observed strong peaks for Cu, Sn, and O elements come from CuO and SnO_2 components in the hybrid nanobelts, whereas the additional Ni and C elemental peaks originate from the nickel grid coated with carbon film used in the HRTEM measurements. In addition, the molar ratio of CuO and SnO_2 is determined to be *ca.* 1.15:1 based on the EDS analysis. Moreover, the HRTEM image (Fig. 3d) clearly reveals four types of lattice fringes with lattice spacings of *ca.* 0.17, 0.33, 0.26, and 0.24 nm, corresponding to (020) plane of CuO nanobelt, (110), (101), and (200) planes of SnO_2 nanocrystals, respectively.
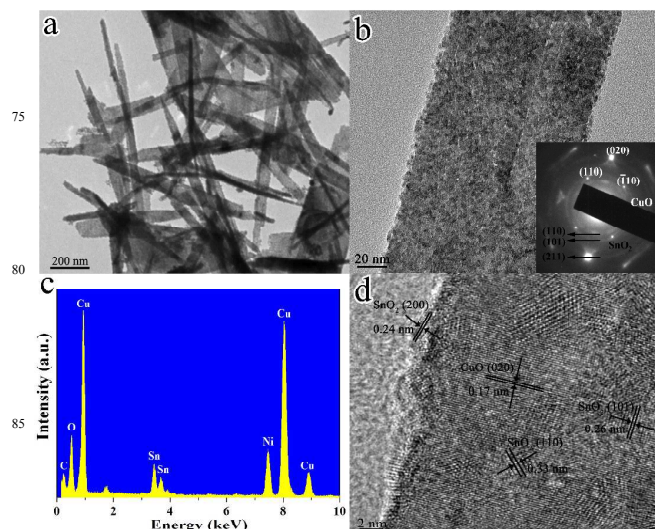
Fig. 3 Morphological, structural and compositional characterizations of $CuO@SnO_2$ nanobelts: (a) TEM image, (b) magnified TEM image with its SAED pattern (inset), (c) EDS spectrum, and (d) HRTEM image.
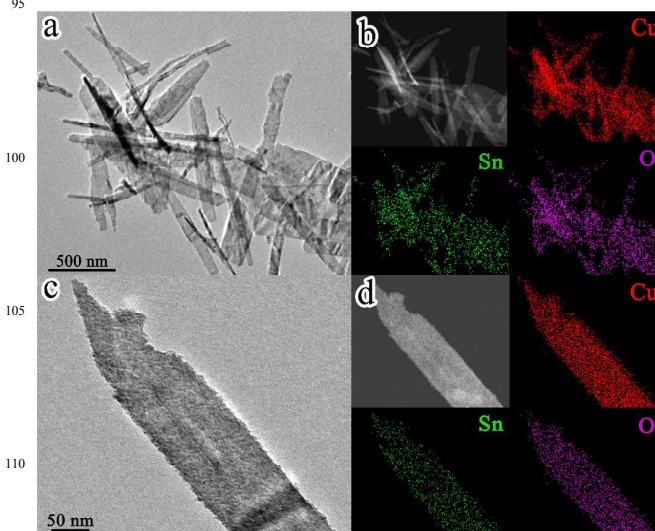
Fig. 4 TEM images (a,c) together with their corresponding dark-field TEM images and EDS elemental mappings of Cu (red), Sn (green), and O (purple) of $CuO@SnO_2$ nanobelts (b,d).

Fig. 4 shows the TEM images together with their corresponding dark-field TEM images and EDS elemental maps of Cu (red), Sn (green), and O (purple) of the CuO@SnO$_2$ nanobelts. As can be seen, the copper, tin, and oxygen elemental signals are evenly distributed within the selected area of multiple nanobelts (Fig. 4a and b) and a magnified nanobelt (Fig. 4c and d), and these elemental distributions are in accordance with the TEM images. These TEM-EDS elemental mapping results further demonstrate the uniform distribution of SnO$_2$ nanocrystals on the surface of CuO nanobelts.
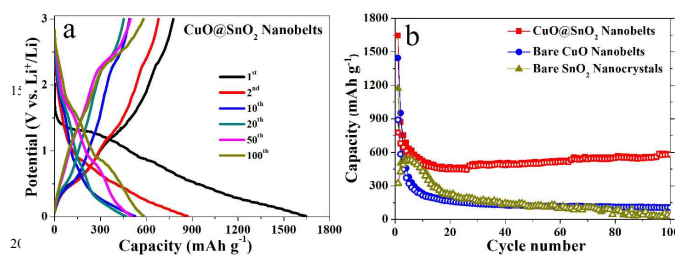
Fig. 5 Lithium storage capabilities of CuO@SnO$_2$ nanobelts, bare CuO nanobelts and SnO$_2$ nanocrystals: (a) discharge and charge curves, and (b) cycling stability.

The as-prepared CuO@SnO$_2$ nanobelts was applied as a potential anode material for LIBs, and its cycling performance was examined in the potential range of 0.01-3 V at a current density of 100 mA g^{-1} in comparison with bare CuO nanobelts and SnO$_2$ nanocrystals (Fig. 5). As observed from Fig. 5a, the voltage plateaus in the discharge/charge curves for CuO@SnO$_2$ nanobelt anode are not obvious, suggesting the combinative electrochemical behavior including the formation/decomposition of polymeric gel-like layer and lithium insertion/extraction in CuO and SnO$_2$, respectively (Fig. S3, ESI†). More interestingly, the capacities of CuO@SnO$_2$ nanobelts experience a gradual increasing process after the initial fading process in the first 20 cycles. In sharp contrast, the capacities of bare CuO nanobelts and SnO$_2$ nanocrystals decrease very fast upon cycling. The synergistic effects between CuO and SnO$_2$ components as well as the unique 1D belt-like nanostructure could be responsible for its markedly enhanced Li-storage capabilities in terms of specific capacity and capacity retention compared with single CuO and SnO$_2$ counterparts.[20-29] For example, the *in-situ* generated Cu nanocrystals during initial lithium-insertion processes can act as effective buffering and conducting matrices and improve the strain accommodation and charge transport capabilities of CuO–SnO$_2$ nanohybrids, and thus the CuO-nanotubes/SnO$_2$ composite[23] and SnO$_2$–CuO Janus-structured nanorods[22] both demonstrate significantly enhanced Li-storage performances in terms of cycling stability and rate capability compared with bare SnO$_2$ anodes. Herein, the *in-situ* generated Cu nanocrystals not only act as effective buffering/conducting matrices, but also serve as efficient catalysts to activate/promote the oxidation of metallic tin[29] and reversible formation/decomposition of polymeric gel-like film on the anodic surface[31] due to the relatively higher operating voltage (3 V) compared with CuO-nanotubes/SnO$_2$ composite (1.5 V)[23] and SnO$_2$–CuO Janus-structured nanorods (1

V),[22] which might be responsible for the higher reversible capacities and capacity-rising phenomena in CuO@SnO$_2$ nanobelts. Additionally, the voltage plateaus at *ca.* 2.5 V in the charge curves become more and more apparent upon cycling, further indicating the existence of probable activation processes of metal oxide components or reversible formation of polymeric gel-like layer (Fig. 5a).[31-33] After 100 cycles, the CuO@SnO$_2$ nanobelt anode is able to deliver a high discharge capacity of 584.3 mA h g^{-1}, which is much higher than those of bare CuO nanobelts (108.1 mA h g^{-1}), SnO$_2$ nanocrystals (28.1 mA h g^{-1}) and the previously reported CuO-nanotubes/SnO$_2$ composite ($\sim$350 mA h g^{-1} in the 20th cycle at 50 mA g^{-1})[23] and SnO$_2$–CuO Janus-structured nanorods ($\sim$392 mA h g^{-1} in the 50th cycle at 3000 mA g^{-1}).[22] The high reversible capacities and remarkable cycling stability of CuO@SnO$_2$ nanobelts make it a promising anode material in advanced LIBs with high energy density and long cycle life.

After 100 cycles, the morphological and compositional features of CuO@SnO$_2$ nanobelt anode in a de-lithiated state (3.0 V *vs.* Li$^+$/Li) were further characterized in comparison with bare CuO nanobelts and SnO$_2$ nanocrystals. Fig. 6 shows the TEM image and its corresponding dark-field TEM image and EDS elemental maps of Cu (red), Sn (green), and O (purple) for CuO@SnO$_2$ nanobelts. As can be seen from the TEM image, the de-lithiated product still manifests a belt-like morphology and is composed of numerous ultrafine nanoparticles. Additionally, the Cu, Sn, and O elemental signals are still uniformly spread over the entire nanobelt. In sharp contrast, the belt-like morphology of bare CuO sample and porous spherical morphology of bare SnO$_2$ sample are not preserved after repeated lithium insertion/extraction (Fig. S4 and S5, ESI†). The de-lithiated CuO and SnO$_2$ products become larger and agglomerated after cycling, and the EDS elemental mappings also demonstrate the nonuniform distribution of Cu and Sn signals within the chosen region. These results confirm the structural stability of bare CuO nanobelts and SnO$_2$ nanocrystals has been significantly enhanced by constructing CuO@SnO$_2$ nanobelts, which can further explain the huge differences in Li-storage capabilities of CuO@SnO$_2$ nanobelts and bare CuO and SnO$_2$ samples.
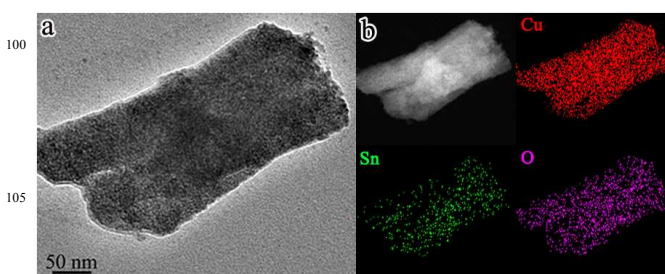
Fig. 6 Morphological and compositional characterizations of CuO@SnO$_2$ nanobelts in a de-lithiated state (3.0 V *vs.* Li$^+$/Li) after 100 cycles: (a) TEM images, and (b) dark-field TEM image and its corresponding EDS elemental mappings of Cu (red), Sn (green), and O (purple).

Conclusions

In summary, we have designed and synthesized novel CuO@SnO$_2$ nanobelts through a facile hydrothermal approach by using CuO nanobelts as templates. Compared with single CuO and SnO$_2$ counterparts, the as-prepared CuO@SnO$_2$ nanobelts exhibits much higher capacities and markedly improved capacity retention by virtue of its unique compositional and structural features. For example, a high reversible capacity of 584.3 mA h g^{-1} could be delivered after 100 cycles in CuO@SnO$_2$ nanobelt anode at a current density of 100 mA g^{-1}. The facile synthetic methodology and remarkable Li-storage performance of CuO@SnO$_2$ nanobelts facilitate its practical application as a high-capacity and long-life anode material for advanced LIBs.

Acknowledgments

Notes and references

Jiangsu Key Laboratory of New Power Batteries, Jiangsu Collaborative Innovation Center of Biomedical Functional Materials, School of Chemistry and Materials Science, Nanjing Normal University, Nanjing 210023, PR China. Fax: +86–25–85893286; Tel: +86–25–85891651; E-mail: zjuwuping@njnu.edu.cn

†Electronic Supplementary Information (ESI) available: [Detailed experimental procedures]. See DOI: 10.1039/b000000x/

‡ Footnotes should appear here. These might include comments relevant to but not central to the matter under discussion, limited experimental and spectral data, and crystallographic data.

1   Y. Idota, T. Kuboka, A. Matsufuji, Y. Maekawa and T. Miyasaka, *Science*, 1997, **276**, 1395.
2   X. M. Zheng, L. Huang, Y. Xiao, H. Su, G. L. Xu, F. Fu, J. T. Li, S. G. Sun, *Chem. Commun.*, 2012, **48**, 6854.
3   F. S. Ke, L. Huang, B. C. Solomon, G. Z. Wei, L. J. Xue, B. Zhang, J. T. Li, X. D. Zhou and S. G. Sun, *J. Mater. Chem.*, 2012, **22**, 17511.
4   X. L. Wang, W. Q. Han, J. Chen and J. Graetz, *ACS Appl. Mater. & Interfaces*, 2012, **2**, 1548.
5   X. L. Wang, H. Y. Chen, J. Bai and W. Q. Han, *J. Phys. Chem. Lett.*, 2012, **3**, 1488.
6   J. Li, P. Wu, Y. Tang, X. Xu, Y. Zhou, Y. Chen and T. Lu, *CrystEngComm*, 2013, **15**, 10340.
7   J. Zai, X. Qian, K. Wang, C. Yu, L. Tao, Y. Xiao and J. Chen, *CrystEngComm*, 2012, **14**, 1364.
8   M. He, L. X. Yuan and Y. H. Huang, *RSC Adv.*, 2013, **3**, 3374.
9   L. Zhuo, Y. Wu, L. Wang, Y. Yu, X. Zhang and F. Zhao, *RSC Adv.*, 2012, **2**, 5084.
10   J. S. Chen and X. W. Lou, *Small*, 2013, **9**, 1877.
11   X. Xia, S. Li, X. Wang, J. Liu, Q. Wei and X. Zhang, *J. Mater. Sci.*, 2013, **48**, 3378.
12   L. Ji, Z. Lin, B. Guo, A. J. Medford and X. Zhang, *Chem. Eur. J.*, 2010, **16**, 11543.
13   P. Wu, N. Du, H. Zhang, J. Yu and D. Yang, *J. Phys. Chem. C*, 2010, **114**, 22535.
14   P. Wu, N. Du, H. Zhang, J. Yu, Y. Qi and D. Yang, *Nanoscale*, 2011, **3**, 746.
15   Q. Han, J. Zai, Y. Xiao, B. Li, M. Xu and X. Qian, *RSC Adv.*, 2013, **3**, 20573.
16   Y. J. Hong, M. Y. Son and Y. C. Kang, *Adv. Mater.*, 2013, **25**, 2279.
17   P. Wu, N. Du, H. Zhang, C. Zhai and D. Yang, *ACS Appl. Mater. & Interfaces*, 2011, **3**, 1946.
18   J. Li, P. Wu, Y. Ye, H. Wang, Y. Zhou, Y. Tang and T. Lu, *CrystEngComm*, 2014, **16**, 517.
19   L. Chen, P. Wu, H. Wang, Y. Ye, B. Xu, G. Cao, Y. Zhou, T. Lu and Y. Yang, *J. Power Sources*, 2014, **247**, 178.
20   J. S. Chen, C. M. Li, W. W. Zhou, Q. Y. Yan, L. A. Archer and X. W. Lou, *Nanoscale*, 2009, **1**, 280.
21   W. Zhou, C. Cheng, J. Liu, Y. Y. Tay, J. Jiang, X. Jia, J. Zhang, H. Gong, H. H. Hng, T. Yu and H. J. Fan, *Adv. Funct. Mater.*, 2011, **21**, 2439.
22   S. H. Choi and Y. C. Kang, *Nanoscale*, 2013, **5**, 4662.
23   C. Li, W. Wei, S. Fang, H. Wang, Y. Zhang, Y. Gui and R. Chen, *J. Power Sources*, 2010, **195**, 2939.
24   X. Y. Xue, Z. H. Chen, L. L. Xing, S. Yuan and Y. J. Chen, *Chem. Commun.*, 2011, **47**, 5205.
25   X. Y. Xue, B. He, S. Yuan, L. L. Xing, Z. H. Chen and C. H. Ma, *Nanotechnology*, 2011, **22**, 395702.
26   Y. Li, Y. Hu, H. Jiang, X. Hou and C. Li, *CrystEngComm*, 2013, **15**, 6715.
27   Z. Fang, J. Huang, W. He, X. Zhang, Y. Wu and J. Qing, *Electrochim. Acta*, 2013, **109**, 454.
28   H. Guo, L. Liu, T. Li, W. Chen, Y. Wang and W. Wang, *Chem. Commun.*, 2014, **50**, 673.
29   C. Hua, X. Fang, Z. Wang and L. Chen, *Chem. Eur. J.*, 2014, **20**, 5487.
30   P. Poizot, S. Laruelle, S. Grugeon, L. Dupont and J. M. Tarascon, *Nature*, 2000, **407**, 496.
31   L. Su, Z. Zhou and P. Shen, *J. Phys. Chem. C*, 2012, **116**, 23974.
32   P. Wu, N. Du, H. Zhang, J. Yu, D. Yang, *J. Phys. Chem. C*, 2011, **115**, 3612.
33   X. Xu, R. Cao, S. Jeong and J. Cho, *Nano Lett.*, 2012, **12**, 4988.